ACS SENSORS

Open Access
This article is licensed under CC-BY-NC-ND 4.0

pubs.acs.org/acssensors
Article

An Underwater Methane Sensor Based on Laser Spectroscopy in a Hollow Core Optical Fiber

Jason A. Kapit,* Sarah Youngs, William A. Pardis, Alexandra M. Padilla, and Anna P. M. Michel

Cite This: ACS Sens. 2024, 9, 5896−5905
Read Online

ACCESS | Metrics & More | Article Recommendations | Supporting Information

ABSTRACT: Existing sensors for measuring dissolved methane in situ suffer from excessively slow response times or large size and complexity. The technology reported here realizes improvements by utilizing a hollow core optical fiber (HFC) as the detection cell in an underwater infrared laser spectrometer. The sensor operates by using a polymer membrane inlet to continuously extract dissolved gas from water. Once inside the sensor, the gas passes through an HCF, within which tunable diode laser spectroscopy is used to quantify methane. The use of an HCF for the optical cell enables advantages of sensitivity, selectivity, compactness, response time, and ease of integration. A submersible prototype has been developed, characterized in the laboratory, and tested in the ocean to a depth of 2000 m. Initial laboratory environmental testing showed a pCH_4 detection range up to 10,000 μatm, an uncertainty of 5.6 μatm or ±1.4% (whichever is greater) and a response time of 4.6 min over a range of controlled operating conditions. Operation at sea demonstrated its utility in generating dissolved methane maps, targeted point sampling, and water column profiling.

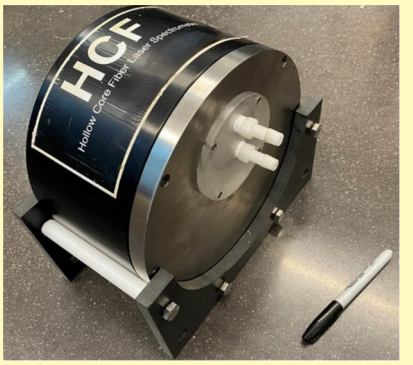

KEYWORDS: *methane, sensor, hollow core fiber, underwater, ocean*

Technologies for measuring methane in Earth's water systems are necessary for numerous areas of oceanographic and environmental research. Most notably, since methane contains 28 times[1] the warming potential of carbon dioxide, there are ongoing efforts to study the roles of oceans, seas, lakes, and wetlands in the global methane budget.[1−5] Recent studies of methane in natural waters have focused on a range of sources including ocean vents, seeps, hydrates, arctic permafrost, and agricultural wetlands.[6−9] In addition to climate considerations, methane-rich sites in the deep ocean support chemosynthetic life. Thus, methane can serve as a ubiquitous chemical tracer for discovering new hydrothermal ecosystems and understanding their associated ecology.[10,11]

Despite a broad application space, most measurements for methane in water are still performed slowly and laboriously via field sampling followed by headspace analysis using large benchtop instruments such as gas chromatographs and laser spectrometers.[10,12−14] Accordingly, there is increasing interest for in situ underwater methane sensors that are efficient, compact, and easy to carry to the field or deploy in situ.

Sensing technologies currently marketed for underwater methane detection include those based on metal-oxide semiconductors (METS), nondispersive infrared sensing (NDIR), and tunable diode laser spectroscopy (TDLAS).[15,16] While these products have demonstrated the potential of underwater methane sensing, each exhibit substantial trade-offs, and broad adoption among the scientific community has been slow. While METS and NDIR sensors can be small and cost-effective, they also exhibit cross-sensitivities to water vapor, temperature, and other hydrocarbons. In contrast, TDLAS methods have good selectivity and sensitivity, but they generally result in large instruments, can have excessively long response-times,[17] or are potentially cost prohibitive.

In addition to commercial sensors, several research groups have developed more customized methane sensors.[11,18−20] Recently, a submersible methane sensor based on optical feedback cavity-enhanced absorption spectroscopy was developed and demonstrated.[21] While the sensor was very sensitive and had a fast response time, its large size and complexity are still potential risks for widespread utility.

Here, we report on the initial development and testing of a new dissolved methane sensor named the Sensor for Aqueous Gases in the Environment (SAGE), which attempts to balance common desirable performance parameters including response time, sensitivity, selectivity, size, robustness, and simplicity. While this initial design targeted deep sea exploration, the technology is adaptable to a broad range of oceanographic and environmental research.

Received: June 25, 2024
Revised: October 1, 2024
Accepted: November 5, 2024
Published: November 11, 2024

ACS Publications
© 2024 The Authors. Published by American Chemical Society

https://doi.org/10.1021/acssensors.4c01563
ACS Sens. 2024, 9, 5896−5905

EXPERIMENTAL SECTION

Sensor Overview. SAGE is based on TDLAS, and compared to existing technologies, it realizes advantages by utilizing a new kind of hollow-core optical fiber (HCF) for its gas detection cell. During operation, SAGE continuously extracts gas from seawater flowing past a polymer membrane inlet, and once inside the sensor, the gas flows into a small headspace and then through an HCF (Figure 1). Simultaneously, light from a fiber-pigtailed laser is coupled into the HCF, and TDLAS is used to detect the gas's methane concentration. Gas flow through the HCF is facilitated by ensuring the exit end of the HCF in the sensor housing is maintained at low pressure.

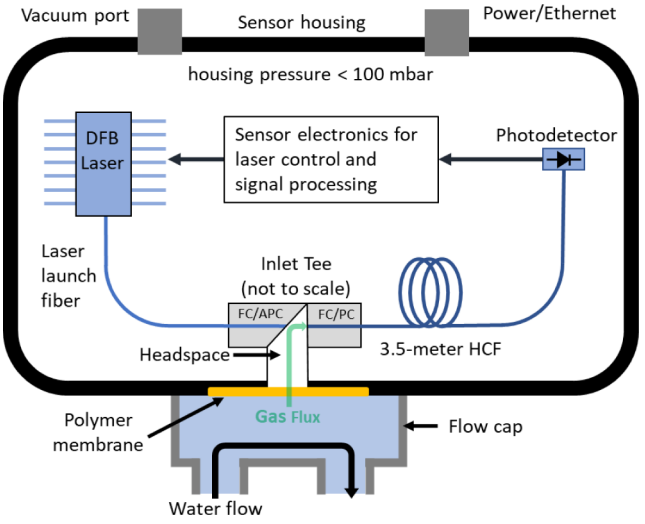

Figure 1. A conceptual diagram of the SAGE sensor. Water is pumped through a flow cap where gas is extracted by a polymer membrane inlet into a headspace. From there, the gas enters an HCF where light from a 1650.9 nm distributed-feedback (DFB) laser is used to detect the amount of methane using TDLAS.

A prototype sensor has been designed, fabricated, and packaged in a housing for deployments of up to 2,500 m. Laboratory experiments were performed to calibrate and characterize its performance, and it was tested at sea during an expedition to the Guaymas Basin in the Gulf of California in November 2021.

Tunable Diode Laser Spectroscopy. SAGE utilizes TDLAS, a common optical technique for sensitive and selective detection of trace gases in the environment. In TDLAS sensors, light from a wavelength-tunable laser is sent through an optical cell (in this case a HCF) containing the sample gas to be measured, and the amount of transmitted light is received by a photodetector. Since the wavelength of the laser is selected to target an absorption line of the gas(es) of interest, the amount of light received by the photodetector is proportional to gas concentration as described by the Beer–Lambert Law:

$$\frac{I(\nu, T, P)}{I_0(\nu)} = \exp\left(\frac{-\mathrm{X}Pl}{kT} S(T) f(\nu, T, P)\right) = \exp(-A(\nu, T, P))$$

Here, I_0 is the incident light intensity from the laser before it enters the HCF, I is the transmitted intensity received by the photodetector, X is the mole fraction of the target gas, P is the total gas pressure, l is the distance light travels through the sample gas, T is the gas temperature, S is the absorption line strength, f is the line shape function, and k is the Boltzmann constant. The parameters I_0, I, and f are all functions of wavenumber, ν. Additionally, I and f are functions of pressure and temperature, and S is also a function of just temperature. Both the line shape and line intensity can be calculated for a specific absorption line using parameters obtained from a molecular absorption database such as HITRAN.[22,23]

For typical direct absorption sensing methods, the wavelength of the laser is repeatedly scanned across the selected absorption feature, and the acquired photodetector signal is converted into an absorbance spectrum, A, containing a peak for which the height is proportional the amount of target gas.

Hollow-Core Optical Fibers. The architecture of SAGE is fundamentally similar to other TDLAS sensors, with the exception of a traditional "free-space" optical cell having been replaced by an HCF. Several recent works review the theory, operation, and uses of HCFs in trace gas sensing applications.[24−26]

As previously illustrated,[27] incorporating an HCF into a TDLAS sensor presents several advantages. Most importantly, it enables a long light-gas interaction length (i.e., high sensitivity) while requiring a very small sample volume. This is advantageous because gas transfer from the water through the membrane is typically slow, and the sensor's response time can be reduced by minimizing the amount of gas that needs to be extracted. Due to the small size of fiber optic components, an HCF gas cell can also be mechanically interfaced to the membrane inlet with minimal addition of headspace volume. Both these aspects aid in reducing the total amount of gas needed to fill the sensor, thereby minimizing the response time.

Other advantages of using an HCF include robust and easy integration using standard fiber optic components, operation at common near-infrared wavelengths, and the elimination of highly precise free-space optical cells.

Gas Mass Transfer. Since TDLAS senses the gas phase, adapting it for dissolved gas measurements first requires extracting gas from the dissolved phase and into a headspace where it can enter the HCF and be optically detected. In SAGE, this extraction is achieved with a polymer membrane inlet using similar methods to previous works.[28−30] Such inlets are typically constructed from a gas permeable and water impermeable polymer, such as Teflon AF or PDMS (polydimethylsiloxane), and to withstand hydrostatic pressure, the membrane is reinforced with a stainless steel mesh or a sintered frit. A conceptual model of the mass transfer through the membrane and the HCF in SAGE is provided in Supporting Information Section S1.

Overall, the design can be optimized by utilizing a highly permeable membrane (i.e., thin, large surface area, and high gas permeability), along with a fiber length that achieves the required sensitivity. Simultaneously, it is desirable to ensure the gas in the headspace is in close equilibration with the gas in the water under steady-state conditions. Though higher equilibration and higher sensitivity can both be achieved by increasing fiber length, this comes at the expense of increasing response time due to the time for gas to fill the fiber. As a result, there is an inherent trade-off between sensitivity, level of gas equilibration, and response time that can be optimized for different applications.

https://doi.org/10.1021/acssensors.4c01563
ACS Sens. 2024, 9, 5896−5905

Calculation of Dissolved Gas Concentration. SAGE determines the partial pressure of dissolved methane in water through the following process. First, the mole fraction of methane, X_{CH4}, in the HCF can be expressed in terms of the peak measured absorbance, A_{peak}, as

$$\chi_{CH4} = \frac{A_{\text{peak}} k T_f}{P_f L_f S(T_f) f_{\text{peak}}(T_f, P_f)} = A_{\text{peak}} \cdot m(T_f, P_f)$$

where T_f and L_f are the temperature and length of the fiber respectively, and P_f is taken to be the average of the pressures at both ends of the fiber (For SAGE, these pressures are the headspace pressure, P_h, and the housing pressure at the fiber outlet, P_o). As noted previously, the parameters S and f can be determined from HITRAN spectroscopic models. Combining parameters also allows X_{CH4} to be written simply as A_{peak} times a scaling factor m, which is only dependent on the pressure and temperature in the fiber.

Next, the assumptions are made that the mole fraction of methane in the fiber is equal to that in the headspace, and that the partial pressure of methane in the headspace, p_h, is simply $X_{CH4}P_h$. In addition, an experimentally determined membrane efficiency constant, e_m, is utilized to account for the difference between the gas partial pressures in the water (p_w) and in the headspace (p_h). Thus, the resulting expression for the partial pressure of methane in the water, pCH_4, is

$$p_w = pCH_4 = e_m P_h \chi_{CH4} = e_m P_h A_{\text{peak}} \cdot m(T_f, P_f)$$

Though SAGE measures the partial pressure of dissolved methane, a quantity often desired from a chemical perspective is the concentration in mol/L, and this conversion can be performed using Henry's Law for methane under various conditions.[31−36]

Engineering Design. The details of the engineering design are described in Supporting Information Section S2.

Dissolved Gas Standards. The methane sensing performance of the SAGE prototype was initially assessed through a series of controlled laboratory calibration and characterization experiments. Calibration gases of methane in air (GASCO, Oldsmar, Florida, 2% accuracy) were used for dry and dissolved gas standards. To create the dissolved standards, the calibration gas was dissolved in tap water using a "shower head" equilibrator that was connected in a water circulation loop with the sensor flow cell. As a result, the sample water circulating past the sensor was also continuously passing through the equilibrator, which enabled full equilibration to be maintained over long timeframes. When increasing from low to high concentration, full equilibration was identified by monitoring the SAGE signal until it had fully stabilized. For all experiments, it was assumed that ambient pressure in the laboratory was 1.0 atm such that water equilibrated with 1000 ppm of CH_4 calibration gas resulted in a 1000 μatm pCH_4 standard. During the experiments, the ambient temperature ranged from 21−25 C, the internal housing pressure ranged between 50−60 mbar, and the flow rate of water past the membrane inlet was 5 L/min, unless stated otherwise.

RESULTS AND DISCUSSION

Optics Calibration. An initial calibration of the optics to determine m was performed by flowing dry methane calibration gases past the sensor inlet without the membrane present. The gas concentrations used were zero air followed by methane concentrations of 1 ppm, 4 ppm, 10 ppm, 100 ppm, 1000 ppm, and 10,000 ppm.

The measured value of A_{peak} for each concentration step is shown in Figure 2 (Top). The results show that SAGE's optics, while operating under steady laboratory conditions, can respond to changes in methane over short timeframes from approximately 1 ppm to at least 10,000 ppm. Figure 2 (Bottom) also shows the average signal for each concentration step in comparison with the methane concentration. The signal response is linear from approximately 10−10,000 ppm. At lower concentrations the response flattens, indicating a lower detection limit of around 4 ppm. From this data, a value of m at room temperature and 525 mbar average fiber pressure, was found to be 7537 ± 62 ppm. This value, along with the measured headspace pressure, was then used to determine the pCH_4 in the headspace.

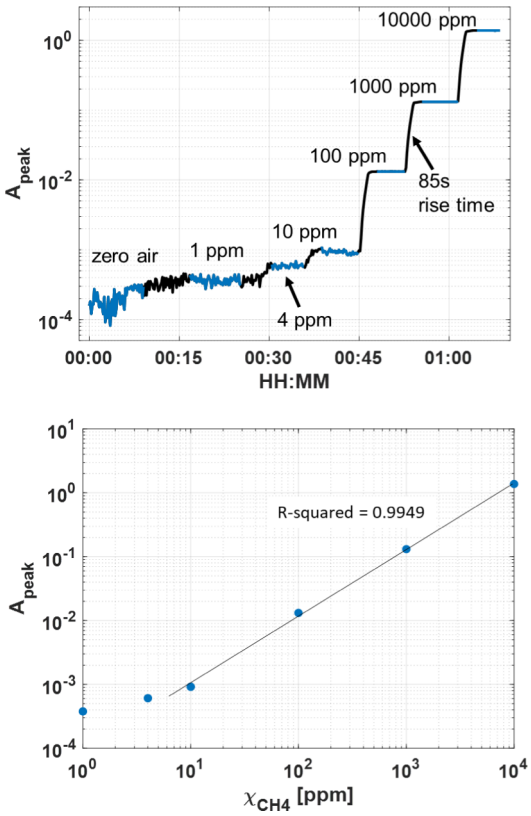

Figure 2. (Top) A calibration performed by introducing dry gases of increasing methane concentration directly into SAGE without the membrane inlet installed. (Bottom) The calibration curve obtained from the same experiment showing A_{peak} versus methane concentration.

The time it takes for gas to flush through the fiber can also be determined from this data by measuring the time for the signal to step from 100 to 1000 ppm in Figure 2 (Top). The rise time for this step was approximately 85 s, and this value represents a lower limit for the sensor's response time when utilizing an HCF of this length (3.5 m) prior to any membrane effects.

Membrane Efficiency. A single point dissolved gas calibration was performed for determining the membrane efficiency parameter, e_m, required for converting the partial pressure of methane in the headspace to the pCH_4 of the water. This calibration was performed with the membrane

https://doi.org/10.1021/acssensors.4c01563
ACS Sens. 2024, 9, 5896−5905

installed and by circulating 1000 μatm pCH_4 equilibrated water past the sensor. Once the signal stabilized, the methane partial pressure in the headspace, p_h, measured 920.2 ± 0.9 μatm, resulting in an e_m value of 1.09 for converting p_h to the pCH_4 of the water. Another way of expressing this is that p_h = 0.92 p_w, or that the membrane is 92% efficient. This value is expected to vary with environmental conditions such as temperature, pressure, and flow rate past the membrane, and one of the purposes of the following experiments was to help assess the magnitude these effects.

Lower Detection Limit. SAGE's lower detection limit is influenced by the well-known effect of higher-order-mode (HOM) interference in HCFs.[37−39] This optical effect is due to the superposition of many weak interference fringes that create small oscillations in the absorbance spectrum, and these oscillations typically shift with changes in the fiber temperature or internal pressure. As a result, small changes in fiber temperature or pressure will cause the fringes to shift and thereby cause the value of A_{peak} to oscillate.

To assess this effect in SAGE, an experiment was performed by measuring room air (~2 μatm CH_4), which was close enough to the sensor's lower detection such that the absorbance spectrum was dominated by the HOM fringes. During the test, the sensor was transferred into a cold room, and the temperature was decreased from 23 to 9 °C to cause the fringes to shift. Figure 3 shows the methane partial pressure in the headspace, p_h, recorded during the test.

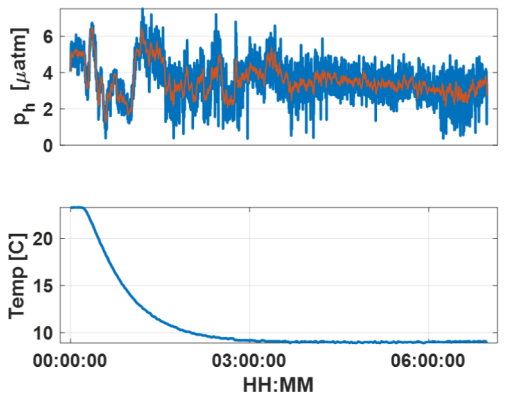

Figure 3. Signal for methane partial pressure in the inlet headspace while ambient temperature was decreased from 23 to 9 °C. This test was performed while monitoring room air without the membrane present.

Oscillatory variations were observed in the signal during the temperature drop. The nonmonotonic nature of this drift, as well as inspection of the absorption spectra during the test, are both consistent with shifts of HOM fringes. During the second half of the experiment, both the temperature and the signal were more stable suggesting the sensor's lower detection limit may be improved under more temperature-controlled conditions. However, as SAGE is intended to function in dynamic environments, the lower detection limit is currently expressed as the largest signal drift during this test, which is ±2.8 μatm, or a magnitude of 5.6 μatm.

Stability. SAGE's stability was assessed by performing three experiments for which water containing 1000 μatm pCH_4 was continuously flowing past the sensor. For the first test, the long-term stability was assessed by monitoring the signal for 65 h under ambient laboratory conditions (Figure 4). For the

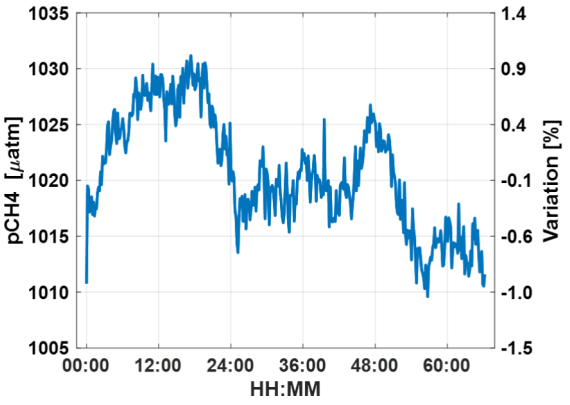

Figure 4. Sensor pCH_4 signal during a test in which 1000 μatm pCH_4 water was circulated past the sensor for 65 h. The largest variations at hours 12 and 48 were identified to coincide with room temperature fluctuations.

second test, the temperature stability was measured by placing SAGE, along with the equilibrator and pumps, on a movable cart and transferring whole setup, while running, into a cold room (Figure 5). During both tests, the signal varied by as much as 1.0% from its mean, and the average signal level did not trend appreciably up or down.

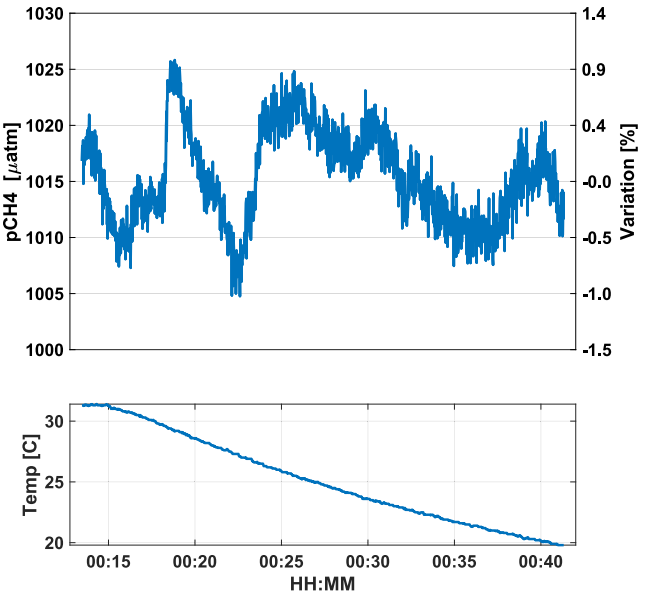

Figure 5. Signal recorded while the temperature of whole experimental setup was decreased from 31 to 20 °C. Experimental limitations prevented reducing the temperature below 20 °C, and similar experiments to colder temperatures should be performed in the future.

Two conclusions can be drawn from these results. First, the signal oscillations with temperature during both tests suggests the main source of instability is once again due to HOM interference. However, the oscillations are larger than when previously measuring the weak signal for the lower detection limit test (±10 μatm vs ±2.8 μatm). This suggests it is not just the amplitude of the shifting fringes directly affecting A_{peak}, but also their effect on the algorithms used for calculating the absorbance (e.g., the baseline determination when calculating A_{peak}).

https://doi.org/10.1021/acssensors.4c01563
ACS Sens. 2024, 9, 5896−5905

A final consideration for long-term stability is the slow rise in the housing's internal pressure as it fills with gas extracted from the water during operation. To assess this effect, a third stability test was performed by initially vacuuming the housing internal pressure down to 50 mbar. Next, the housing pressure relief valve was manually vented several times to increase the internal pressure from 100 mbar to 500 mbar in steps of 100 mbar, and the result is shown in Figure 6.

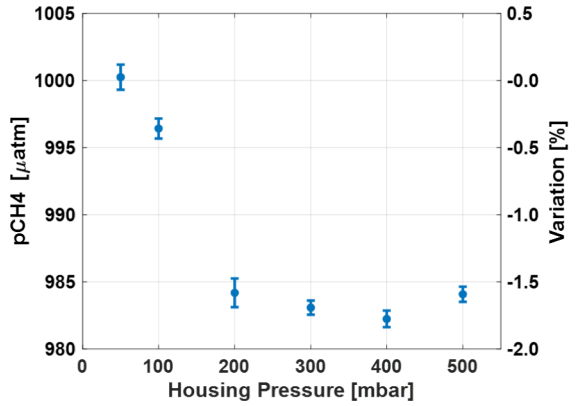

Figure 6. Sensor pCH_4 signal during a test in which 1000 μatm pCH_4 water was circulated past the sensor, and the housing pressure was increased from 50 mbar to 500 mbar. The variation in the signal is as much as −1.8%.

The total signal change over the full experiment was −1.8%, most of which occurred at housing pressures above 100 mbar. The change could be due to both shifts in the HOM fringes as well as the effect of increasing gas pressure on the spectroscopy. Nevertheless, the relatively small overall change indicates pressure in the housing is well compensated for through the HITRAN pressure corrections.

In addition to characterizing stability, these tests can be used to assess how fast gas is building up in the housing, and thus, how long the sensor can operate without the housing pressure affecting the signal by more than 1.8%. The pressure rise during the 65-h test was 5.5 mbar/day, indicating that if the housing pressure is restricted to <500 mbar, a deployment would be limited to ∼82 days. Efforts are currently underway to study the feasibility of incorporating an internal pump to dispel gas out of the housing to allow for longer-term operation.

Response Time. The sensor response time was characterized by adjusting the setup such that water flowing past the membrane could be rapidly switched between two samples, one equilibrated with room air and a second equilibrated with 1000 μatm pCH_4. The response time result for switching from low methane concentration to high is shown in Figure 7.

The 90% response time for the sensor at this temperature is 275 s or 4.6 min at the ambient laboratory temperature of 24 °C. During field deployments, it is expected that colder ocean temperatures would increase this value somewhat since gas diffusivity is proportional to temperature.

Effect of Flow Rate. As indicated in eqs S5 and S7, the water flow rate past the membrane is expected to influence boundary layer thickness and thereby affect the membrane efficiency, e_m. To characterize this effect, 1000 μatm equilibrated water was circulated past the sensor at increasing flow rates from 1 L/min to 10 L/min in increments of 1 L/min. The signal change for each flow rate is shown in Figure 8.

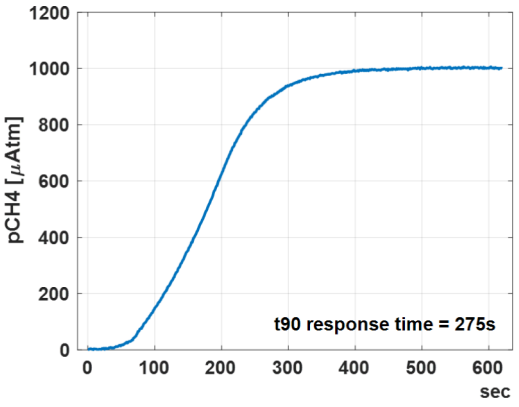

Figure 7. Sensor response time when instantly switching from atmosphere equilibrated water to 1000 μatm pCH4 equilibrated water at 24 °C.

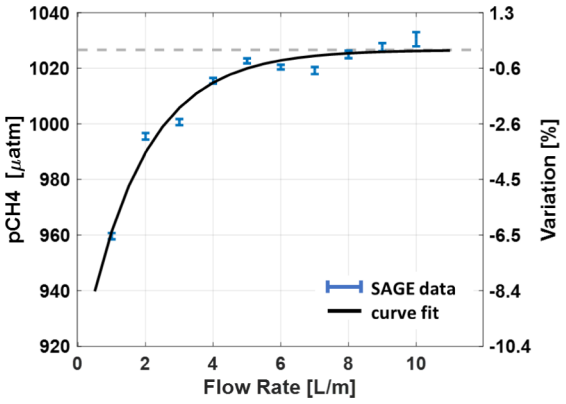

Figure 8. Sensor pCH_4 signal during a test in which 1000 μatm pCH_4 water was circulated past the sensor, and the flow rate was increased from 1 L/min to 10 L/min. The gray line indicates the asymptotic value of the exponential fit, which is used as the reference value for flow rate dependency.

Increasing the flow rate causes the signal to also increase and asymptotically approach a maximum value. At flow rates above 4 L/min the signal is within 1% of this maximum, which indicates that robust flow control above 4 L/min is important for ensuring sensor accuracy.

Standard Uncertainty. An assessment of standard uncertainty was performed by comparing nine instances during the calibration and characterization time frame when the sensor was measuring 1000 μatm pCH_4 water under similar standard conditions (ambient laboratory temperature, a housing pressure of 50 mbar, and a flow rate of 5 L/min) without recalibration. The comparison is shown in Figure 9, for which some points were obtained from the data reported above, and all the results spanned a time frame of 7 weeks. Thus, the comparison provides a good indication of the sensor's uncertainty and repeatability over time.

The results show a relative standard uncertainty across the tests of ±1.4%, and a bias of 19 μatm. It is possible that significant contributions to the bias and uncertainty are not due to the sensor itself, but instead arise from changes in laboratory atmospheric pressure and variations between different bottles of calibration gas.

Potential Interferences. A thorough experimental investigation for interferences from gases other than CH_4 was outside the scope of this prototype development. Nevertheless,

https://doi.org/10.1021/acssensors.4c01563
ACS Sens. 2024, 9, 5896−5905

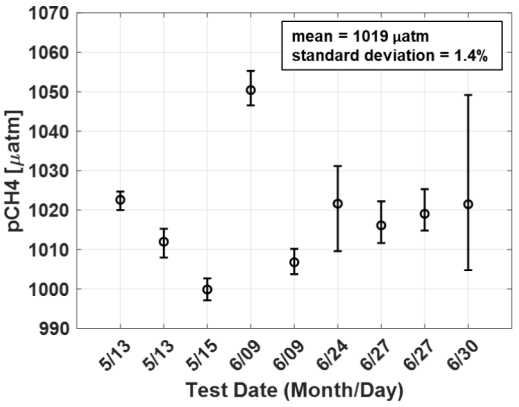

Figure 9. Nine tests over 7 weeks were used to assess sensor uncertainty.

several potential interferences can be identified for future study, most of which arise from significant changes in dissolved gases other than methane.

First, total gas pressure varies in natural waters (for example in oxygen minimum zones and at hydrothermal sites), and it is still necessary to experimentally test the sensor's response to variations in total dissolved gas pressure above or below 1 atm.

Second, the membrane has preferential selectivity to various gases. For example, for a Teflon AF membrane, N_2, O_2, and CO_2 have permeabilities 1.3, 2.9, and 8.2 times that of CH_4. Though the high membrane efficiency should help mitigate adverse selectivity effects, it will be necessary confirm whether changes in the ratio of balance gases away from close-to-atmospheric 80% N_2/20% O_2 affects the signal.

Third, interference from other near-infrared absorbing species should be considered, as they could overlap with the obtained methane spectrum and affect data processing. A preliminary inspection of HITRAN data near 1650.9 nm showed a nearby CO_2 absorption line which is ~2,500 times weaker than the target methane line, and it would be prudent to test whether it interferes at high CO_2 concentrations.

Lastly, the effect of the primary balance gases on the spectroscopic broadening coefficient should be considered. Databases such as HITRAN assume pressure broadening due to air for modeling the line shape, and this is acceptable for many environmental applications. However, if the primary balance gases shift substantially from an N_2/O_2 mixture, the calculations SAGE uses for correcting peak height with pressure may lose accuracy.

All of these effects could be studied by modifying the dissolved gas equilibrator in the future to enable testing of dissolved gas mixtures of CH_4 with air, N_2, and CO_2 as well as by enabling the headspace pressure to be increased or decreased.

Field Tests. The SAGE prototype was field-tested for the first time in November 2021 in the Guaymas Basin in the Gulf of California. This location was selected as a test site due to its widespread hydrothermal activity that includes black smoker vents, diffuse flows, and various forms of deep-sea organisms, all of which cycle copious amounts of methane.[40−42] The expedition was onboard the R/V Roger Revelle (RR2107), and SAGE was demonstrated on three oceanographic platforms including the AUV Sentry, the ROV Jason, and a standard CTD rosette (Figure 10). The primary purpose of this fieldwork was to validate SAGE's utility for ocean exploration at depths down to 2,000 m.

Since AUV Sentry is optimized for deep ocean surveying, it was used to assess SAGE's utility in creating methane maps close to the seafloor. To achieve this, SAGE was mounted on Sentry inside the vehicle body (Figure 10, Left) with a sample water intake tube extending out the side of the vehicle, and an underwater pump connected inline to provide water flow of 4 L/min.

On one of the expedition dives, Sentry and SAGE mapped pCH_4 at an altitude of 4 m above a seafloor feature called Ring Vent (27.506°N, 111.680°W), which is known to contain numerous methane seeps and diffuse flows.[41] To survey the area for methane, Sentry traveled in a standard "lawn mower" path over site at 0.65 m/s with the major track lines extending from the northwest to the southeast. The resulting map, shown in Figure 11 (Left), was created from Ring Vent bathymetry data, Sentry navigation data, and SAGE pCH_4 data. The response time for the SAGE signal was coarsely corrected by implementing a 5 min delay with respect to Sentry's location. The map shows an elevated methane signal of at least 30 μatm over much of the Ring Vent site, along with two methane hot spots to the northwest. This result demonstrates SAGE's utility

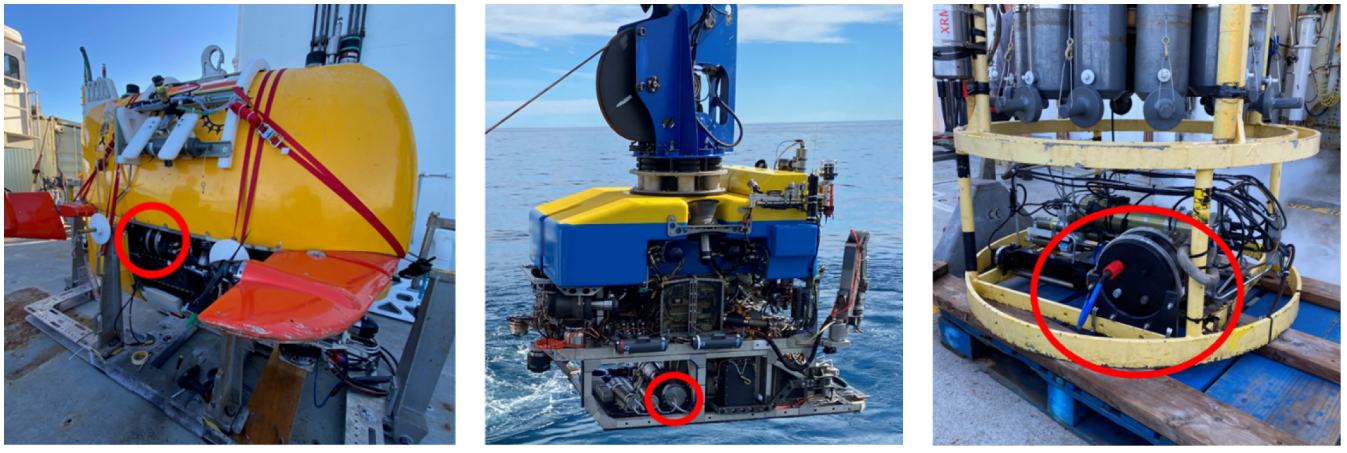

Figure 10. SAGE mounted on three different oceanographic exploration platforms during a research expedition onboard the R/V Roger Revelle to the Guaymas Basin in November 2021.(Left) SAGE mounted on the AUV Sentry. (Center) SAGE mounted on the ROV Jason. (Right) SAGE mounted on the ship's CTD rosette. SAGE is circled in red in each image.

https://doi.org/10.1021/acssensors.4c01563
ACS Sens. 2024, 9, 5896−5905

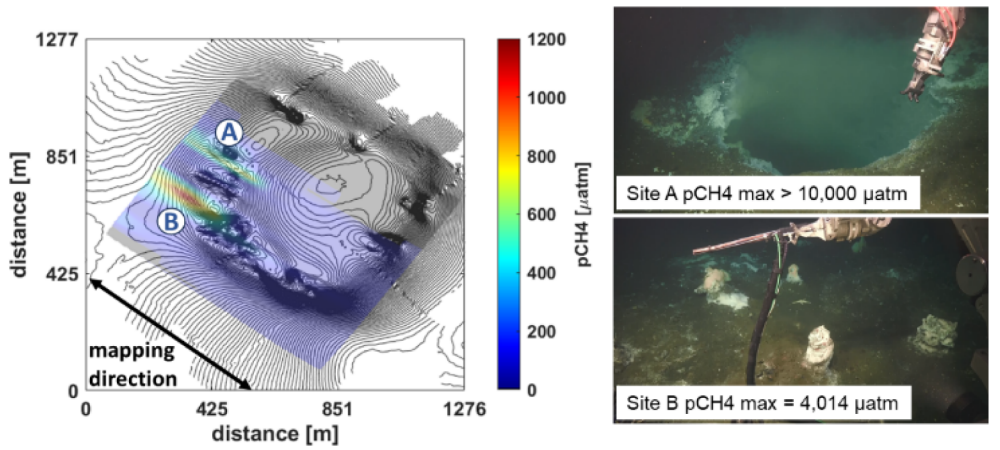

Figure 11. (Left) SAGE was utilized on the AUV Sentry to create a map of methane in the vicinity of a seafloor feature called Ring Vent. The black lines are Ring Vent bathymetry data, and the color is pCH_4. Two methane hotspots A and B were found to the northwest. (Right) The two hotspots were the subject of a more targeted subsequent investigation using ROV Jason.

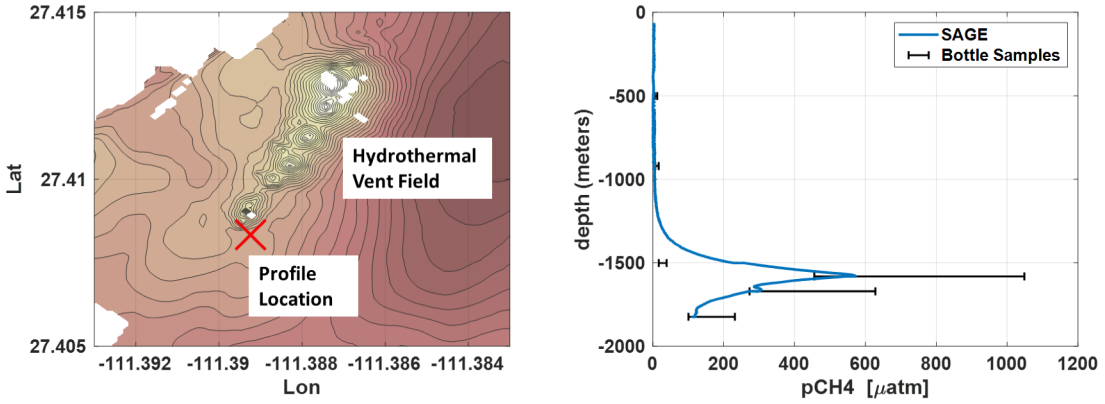

Figure 12. SAGE was installed on the ship's CTD rosette to record a methane profile in the water column through a neutrally buoyant hydrothermal plume.

in mapping dissolved methane over large spatial scales in the water column, as well as identifying regions of high methane emission which warrant more targeted investigation. The elongated shape of the hotspots A and B from the northwest to the southeast is predominantly an artifact due to SAGE's response time and the direction of the vehicle path.

More targeted methane measurements at Ring Vent were also performed on a separate dive when SAGE was installed on the ROV Jason. To achieve this, the sensor was mounted in a back bay of the ROV (Figure 10, Center) and tubing was run from the sensor's flow cap to a sampling wand held by the vehicle manipulator. An inline pump was installed to pull fluid through the sampling wand and back past SAGE. On deck testing indicated this setup consistently achieved fluid flow past the sensor of 3−4 L/min. Though this flow was slower than the desired 4 L/min, it was the maximum that could be achieved using the SBE 5T pump and the long tubing run from the manipulator to the sensor.

During the dive, the ROV mapped methane around the rim of Ring Vent and once again found two locations of highly elevated methane at locations A and B. In addition to viewing the methane signal in real-time from the ship, the ability to actively control the ROV and view real-time video enabled targeted methane measurements at both sites (Figure 11 − Right). At Site A, a large borehole-like feature was found to be emitting a significant diffuse flow of hydrothermal fluid, and as the ROV passed by it, SAGE's methane reading increased above its upper detection limit of 10,000 μatm. The feature was initially speculated to be a borehole from the International Ocean Discovery Program Expedition 385,[43] but a review of the published coring sites could not confirm drilling at precisely that location. At Site B, numerous small chimneys were found, some emitting intermittent diffuse streams of hydrothermal fluid. The surrounding area also contained a variety of bacterial mats, mineral deposits, and fauna. The sensor measurement in the ambient water surrounding this site reached as high as 4014 μatm.

Demonstration of SAGE on a third oceanographic platform was accomplished by installing it on the ship's CTD rosette which could be lowered and raised through the water column to collect a continuous depth profile of methane. To achieve this, SAGE was mounted on an extension at the bottom of the rosette (Figure 10, Right) and powered from the rosette power. Water flow was provided by connecting SAGE in line with the rosette's standard CTD pump, which provided water flow of only ∼1.5 L/min. The site of the cast was specifically chosen so the profile would pass through the neutrally buoyant layer of a hydrothermal plume, at the Guaymas North vent site (27.40834, 111.38924°W) (Figure 12 - Left).

A methane profile was collected on the ascent while rising at a rate of 10 m/min through the water column (Figure 12 - Right). The neutrally buoyant plume layer containing elevated

https://doi.org/10.1021/acssensors.4c01563
ACS Sens. 2024, 9, 5896−5905

levels of methane was clearly present at a depth of 1,580 m. Elevated levels of methane extended fully to the seafloor and dissipated at depths shallower than ∼1,500 m.

To validate the SAGE profile data, six Niskin water bottle samples were also collected during the profile ascent and subsequently analyzed on a Los Gatos Research (LGR) Dissolved Gas Extraction Unit coupled with a LGR Greenhouse Gas Analyzer (GGA). The results agree except for the bottle sample acquired at 1,500 m, which could be due to the response time of the sensor and the slow flow rate, causing it to continue to drop slowly after it had exited the plume. It is notable that the large error bars on the bottle samples exemplify the difficulty of accurately calibrating the GGA extraction efficiency and the uncertainties present when retrieving bottle samples for laboratory analysis. In the future, analysis of bottle samples via gas chromatography would provide a more rigorous comparison than use of the GGA.

CONCLUSIONS

SAGE is a compact dissolved gas sensor capable of detecting dissolved methane in the laboratory and in the ocean at depths down to 2,000 m. Calibrations and characterizations have shown that it can detect methane partial pressure levels up to 10,000 μatm with an uncertainty of 5.6 μatm or ±1.4% (whichever is greater) under a range of controlled laboratory conditions that are also relevant to terrestrial field use (i.e., 10 to 30 °C, 1 atm ambient pressure, and robust flow control). Thus, developing a field-portable system for laboratory use and for terrestrial waters could find immediate applications.

Achieving a robust accuracy assessment for submerged ocean applications was technically challenging and will need to be the subject of future work. Though the pump flow speed on the various platforms could be coarsely measured before deployment, there was no feedback for measuring the actual flow rate underwater on either AUV Sentry or the CTD rosette. When operating on ROV Jason, an in-line flow spinner viewed by a vehicle camera often appeared to slow down or stop, which resulted in significant measurement uncertainty. Additional uncertainty also arose from the unknown effect on the membrane of hydrostatic pressure, which also remains to be characterized.

Nevertheless, once in situ accuracy can be specified with confidence, this work has demonstrated that the sensor's response time of 4.6 min is sufficient for many ocean applications including exploration, plume mapping, targeted point measurements, and depth profiles. Since a response time of 4.6 min would still be considered slow for some AUV mapping purposes, a reasonable strategy may be to utilize SAGE to initially coarsely characterize the location and magnitude of methane features and then subsequently return to those sites for more targeted and accurate measurements. In addition, when profiling, it would likely be necessary to hold the sensor at a fixed depth for ∼5 min to obtain an accurate reading.

Creating additional SAGE units with longer or shorter fibers, or transitioning to mid-infrared wavelengths, would result in sensors more optimized for specific applications such as plume sniffing at background pCH_4 levels (∼2 μatm), isotope studies, and higher resolution mapping. Using lasers and fibers at different wavelengths would also enable detection of other dissolved gases such as carbon dioxide, and ongoing advancements in HCF research could result in lower detection limits (via better HOM rejection) and a smaller sensor (via a smaller bend radius). Nevertheless, even in its current form, SAGE can begin to serve as an additional technology for measuring and mapping methane in Earth's water systems.

ASSOCIATED CONTENT

Supporting Information

The Supporting Information is available free of charge at https://pubs.acs.org/doi/10.1021/acssensors.4c01563.

Supporting Information S1. Contains the theory for modeling the gas mass transfer through the sensor. Supporting Information S2. Contains the engineering details of the components used to construct the prototype sensor (PDF)

AUTHOR INFORMATION

Corresponding Author

Jason A. Kapit − *Woods Hole Oceanographic Institution, Woods Hole, Massachusetts 02543, United States;* orcid.org/0009-0007-6171-1024; Email: jkapit@whoi.edu

Authors

Sarah Youngs − *Woods Hole Oceanographic Institution, Woods Hole, Massachusetts 02543, United States;* orcid.org/0000-0002-1973-7075

William A. Pardis − *Woods Hole Oceanographic Institution, Woods Hole, Massachusetts 02543, United States*

Alexandra M. Padilla − *Woods Hole Oceanographic Institution, Woods Hole, Massachusetts 02543, United States;* Present Address: Cooperative Institute for Research in Environmental Sciences, University of Colorado Boulder, l333 Grandview Ave, Boulder, CO 80302

Anna P. M. Michel − *Woods Hole Oceanographic Institution, Woods Hole, Massachusetts 02543, United States;* orcid.org/0000-0001-9319-0592

Complete contact information is available at: https://pubs.acs.org/10.1021/acssensors.4c01563

Funding

This work was supported by the National Oceanographic and Atmospheric Administration (Award NA18OAR0110354), the Schmidt Marine Technology Partners (Awards G-1801−57413−2018 and G-22−63744), the National Philanthropic Trust/Ocean Kind, and internal funding from the Woods Hole Oceanographic Institution.

Notes

The authors declare no competing financial interest.

REFERENCES

(1) Kort, E. A.; Wofsy, S. C.; Daube, B. C.; Diao, M.; Elkins, J. W.; Gao, R. S.; Hintsa, E. J.; Hurst, D. F.; Jimenez, R.; Moore, F. L.; et al. Atmospheric Observations of Arctic Ocean Methane Emissions up to 82° North. *Nat. Geosci.* **2012**, *5* (5), 318.

(2) Hamdan, L. J.; Wickland, K. P. Methane Emissions from Oceans, Coasts, and Freshwater Habitats: New Perspectives and Feedbacks on Climate. *Limnol. Oceanogr.* **2016**, *61* (S1), S3−S12.

(3) Humborg, C.; Geibel, M. C.; Sun, X.; McCrackin, M.; Mörth, C. M.; Stranne, C.; Jakobsson, M.; Gustafsson, B.; Sokolov, A.; Norkko, A.; Norkko, J. High Emissions of Carbon Dioxide and Methane from the Coastal Baltic Sea at the End of a Summer Heat Wave. *Front. Mar. Sci.* **2019**, *6*, 493.

(4) Matthews, E.; Johnson, M. S.; Genovese, V.; Du, J.; Bastviken, D. Methane Emission from High Latitude Lakes: Methane-Centric Lake Classification and Satellite-Driven Annual Cycle of Emissions. *Sci. Rep.* **2020**, *10* (1), 12465.
(5) Thornton, B. F.; Prytherch, J.; Andersson, K.; Brooks, I. M.; Salisbury, D.; Tjernström, M.; Crill, P. M. Shipborne Eddy Covariance Observations of Methane Fluxes Constrain Arctic Sea Emissions. *Sci. Adv.* **2020**, *6* (5), aay7934.
(6) Bridgham, S. D.; Cadillo-Quiroz, H.; Keller, J. K.; Zhuang, Q. Methane Emissions from Wetlands: Biogeochemical, Microbial, and Modeling Perspectives from Local to Global Scales. *Glob. Change Biol.* **2013**, *19* (5), 1325.
(7) Ruppel, C. D.; Kessler, J. D. The Interaction of Climate Change and Methane Hydrates. *Rev. Geophys.* **2017**, *55* (1), 126.
(8) Weber, T.; Wiseman, N. A.; Kock, A. Global Ocean Methane Emissions Dominated by Shallow Coastal Waters. *Nat. Commun.* **2019**, *10* (1), 4584.
(9) Kleber, G. E.; Hodson, A. J.; Magerl, L.; Mannerfelt, E. S.; Bradbury, H. J.; Zhu, Y.; Trimmer, M.; Turchyn, A. V. Groundwater Springs Formed during Glacial Retreat Are a Large Source of Methane in the High Arctic. *Nat. Geosci.* **2023**, *16* (7), 597.
(10) German, C. R.; Bowen, A.; Coleman, M. L.; Honig, D. L.; Huber, J. A.; Jakuba, M. V.; Kinsey, J. C.; Kurz, M. D.; Leroy, S.; McDermott, J. M.; et al. Diverse Styles of Submarine Venting on the Ultraslow Spreading Mid-Cayman Rise. *Proc. Natl. Acad. Sci. U. S. A.* **2010**, *107* (32), 14020−14025.
(11) Preston, V.; Flaspohler, G.; Kapit, J.; Pardis, W.; Youngs, S.; Martocello, D. E., III; Roy, N.; Girguis, P. R.; Wankel, S. D.; Michel, A. P. M. Discovering Hydrothermalism from Afar: In Situ Methane Instrumentation and Change-Point Detection for Decision-Making. *Front. Earth Sci.* **2022**, *10*, 984355.
(12) Gentz, T.; Damm, E.; Schneider von Deimling, J.; Mau, S.; McGinnis, D. F.; Schlüter, M. A Water Column Study of Methane around Gas Flares Located at the West Spitsbergen Continental Margin. *Cont. Shelf Res.* **2014**, *72*, 107.
(13) Magen, C.; Lapham, L. L.; Pohlman, J. W.; Marshall, K.; Bosman, S.; Casso, M.; Chanton, J. P. A Simple Headspace Equilibration Method for Measuring Dissolved Methane. *Limnol. Oceanogr. Methods* **2014**, *12*, 637.
(14) Roberts, H. M.; Shiller, A. M. Determination of Dissolved Methane in Natural Waters Using Headspace Analysis with Cavity Ring-down Spectroscopy. *Anal. Chim. Acta* **2015**, *856*, 68.
(15) Boulart, C.; Connelly, D. P.; Mowlem, M. C. Sensors and Technologies for in Situ Dissolved Methane Measurements and Their Evaluation Using Technology Readiness Levels. *TrAC - Trends Anal. Chem* **2010**, *29* (2), 186.
(16) Schmidt, M.; Linke, P.; Esser, D. Recent Development in IR Sensor Technology for Monitoring Subsea Methane Discharge. *Mar. Technol. Soc. J.* **2013**, *47* (3), 27.
(17) Dølven, K. O.; Vierinen, J.; Grilli, R.; Triest, J.; Ferré, B. Response Time Correction of Slow-Response Sensor Data by Deconvolution of the Growth-Law Equation. *Geosci. Instrum. Methods Data Syst.* **2022**, *11* (2), 293.
(18) Schlüter, M.; Gentz, T. Application of Membrane Inlet Mass Spectrometry for Online and In Situ Analysis of Methane in Aquatic Environments. *J. Am. Soc. Mass Spectrom.* **2008**, *19* (10), 1395.
(19) Boulart, C.; Prien, R.; Chavagnac, V.; Dutasta, J.-P. Sensing Dissolved Methane in Aquatic Environments: An Experiment in the Central Baltic Sea Using Surface Plasmon Resonance. *Environ. Sci. Technol.* **2013**, *47* (15), 8582−8590.
(20) Yuan, F.; Hu, M.; He, Y.; Chen, B.; Yao, L.; Xu, Z.; Kan, R. Development of an in Situ Analysis System for Methane Dissolved in Seawater Based on Cavity Ringdown Spectroscopy. *Rev. Sci. Instrum.* **2020**, *91* (8), 083106.
(21) Grilli, R.; Triest, J.; Chappellaz, J.; Calzas, M.; Desbois, T.; Jansson, P.; Guillerm, C.; Ferré, B.; Lechevallier, L.; Ledoux, V.; Romanini, D. Sub-Ocean: Subsea Dissolved Methane Measurements Using an Embedded Laser Spectrometer Technology. *Environ. Sci. Technol.* **2018**, *52* (18), 10543−10551.
(22) Gordon, I. E.; Rothman, L. S.; Hill, C.; Kochanov, R. V.; Tan, Y.; Bernath, P. F.; Birk, M.; Boudon, V.; Campargue, A.; Chance, K. V.; et al. The HITRAN2016 Molecular Spectroscopic Database. *J. Quant. Spectrosc. Radiat. Transfer.* **2017**, *203*, 3.
(23) Rothman, L. S. History of the HITRAN Database. *Nat. Rev. Phys.* **2021**, *3* (5), 302.
(24) Belardi, W. Hollow-Core Optical Fibers. *Fibers* **2019**, *7* (5), 50.
(25) Debord, B.; Amrani, F.; Vincetti, L.; Gérôme, F.; Benabid, F. Hollow-Core Fiber Technology: The Rising of "Gas Photonics. *Fibers* **2019**, *7* (2), 16.
(26) Nikodem, M. Laser-Based Trace Gas Detection inside Hollow-Core Fibers: A Review. *Materials* **2020**, *13* (18), 3983.
(27) Kapit, J.; Michel, A. P. M. Dissolved Gas Sensing Using an Anti-Resonant Hollow Core Optical Fiber. *Appl. Opt.* **2021**, *60* (33), 10354.
(28) McNeil, C.; D'Asaro, E.; Johnson, B.; Horn, M. A Gas Tension Device with Response Times of Minutes. *J. Atmos. Ocean. Technol.* **2006**, *23* (11), 1539.
(29) Wankel, S. D.; Huang, Y. W.; Gupta, M.; Provencal, R.; Leen, J. B.; Fahrland, A.; Vidoudez, C.; Girguis, P. R. Characterizing the Distribution of Methane Sources and Cycling in the Deep Sea via in Situ Stable Isotope Analysis. *Environ. Sci. Technol.* **2013**, *47* (3), 1478.
(30) Reed, A.; McNeil, C.; D'Asaro, E.; Altabet, M.; Bourbonnais, A.; Johnson, B. A Gas Tension Device for the Mesopelagic Zone. *Deep-Sea Res. Part Oceanogr. Res. Pap.* **2018**, *139*, 68.
(31) Yamamoto, S.; Alcauskas, J. B.; Crozier, T. E. Solubility of Methane in Distilled Water and Seawater. *J. Chem. Eng. Data* **1976**, *21* (1), 78.
(32) Bonham, L. C. Solubility of Methane in Water at Elevated Temperatures and Pressures: GEOLOGIC NOTES. *AAPG Bull.* **1978**, *62*, 2478−2481.
(33) Wiesenburg, D. A.; Guinasso, N. L. Equilibrium Solubilities of Methane, Carbon Monoxide, and Hydrogen in Water and Sea Water. *J. Chem. Eng. Data* **1979**, *24* (4), 356.
(34) Price, L. C. AQueous solubility of methane at elevated pressures and temperatures. *Am. Assoc. Pet. Geol. Bull.* **1979**, *63* (9), 1527−1533.
(35) Blount, C. W.; Price, L. C. *Solubility of Methane in Water under Natural Conditions: a Laboratory Study. Final Report, April 1, 1978-June 30, 1982*; UNT Digital Library, 1982.
(36) Duan, Z.; Møller, N.; Greenberg, J.; Weare, J. H. The Prediction of Methane Solubility in Natural Waters to High Ionic Strength from 0 to 250°C and from 0 to 1600 bar. *Geochim. Cosmochim. Acta* **1992**, *56* (4), 1451.
(37) Yang, F.; Jin, W.; Cao, Y.; Ho, H. L.; Wang, Y. Towards High Sensitivity Gas Detection with Hollow-Core Photonic Bandgap Fibers. *Opt. Express* **2014**, *22* (20), 24894.
(38) Hu, L.; Zheng, C.; Yao, D.; Yu, D.; Liu, Z.; Zheng, J.; Wang, Y.; Tittel, F. K. A Hollow-Core Photonic Band-Gap Fiber Based Methane Sensor System Capable of Reduced Mode Interference Noise. *Infrared Phys. Technol.* **2019**, *97*, 101−107.
(39) Zhang, E. J.; Tombez, L.; Teng, C. C.; Wysocki, G.; Green, W. M. J. Adaptive Etalon Suppression Technique for Long-Term Stability Improvement in High Index Contrast Waveguide-Based Laser Absorption Spectrometers. *Electron. Lett.* **2019**, *55* (15), 851.
(40) Welhan, J. A.; Lupton, J. E. Light Hydrocarbon Gases in Guaymas Basin Hydrothermal Fluids: Thermogenic versus Abiogenic Origin. *Am. Assoc. Pet. Geol. Bull.* **1987**, *71* (1), 215−223.
(41) Teske, A.; McKay, L. J.; Ravelo, A. C.; Aiello, I.; Mortera, C.; Núñez-Useche, F.; Canet, C.; Chanton, J. P.; Brunner, B.; Hensen, C.; et al. Characteristics and Evolution of Sill-Driven off-Axis Hydrothermalism in Guaymas Basin − the Ringvent Site. *Sci. Rep.* **2019**, *9* (1), 13847.
(42) Teske, A.; Wegener, G.; Chanton, J. P.; White, D.; MacGregor, B.; Hoer, D.; de Beer, D.; Zhuang, G.; Saxton, M. A.; Joye, S. B.; Lizarralde, D.; Soule, S. A.; Ruff, S. E. Microbial Communities Under Distinct Thermal and Geochemical Regimes in Axial and Off-Axis Sediments of Guaymas Basin. *Front. Microbiol.* **2021**, *12*, 633649.

https://doi.org/10.1021/acssensors.4c01563
ACS Sens. 2024, 9, 5896−5905

(43) Teske, A.; Lizarralde, D.; Höfig, T.; Aiello, I. W.; Ash, J. L.; Bojanova, D. P.; Buatier, M. D.; Edgcomb, V. P.; Galerne, C. Y.; Gontharet, S., et al. Expedition 385 summary. In *Proceedings of the International Ocean Discovery Program*; IODP, 2020.

https://doi.org/10.1021/acssensors.4c01563
ACS Sens. 2024, 9, 5896−5905